
Runge-Kutta Approximation and Decoupled Attention for Rectified Flow Inversion and Semantic Editing

Weiming Chen¹ Zhihan Zhu¹ Yijia Wang¹ Zhihai He^{1,2*}

¹Southern University of Science and Technology

²Pengcheng Laboratory

{chenwm2023, 12312326, 12212122}@mail.sustech.edu.cn

hezh@sustech.edu.cn

Abstract

Rectified flow (RF) models have recently demonstrated superior generative performance compared to DDIM-based diffusion models. However, in real-world applications, they suffer from two major challenges: (1) low inversion accuracy that hinders the consistency with the source image, and (2) entangled multimodal attention in diffusion transformers, which hinders precise attention control. To address the first challenge, we propose an efficient high-order inversion method for rectified flow models based on the Runge-Kutta solver of differential equations. To tackle the second challenge, we introduce Decoupled Diffusion Transformer Attention (DDTA), a novel mechanism that disentangles text and image attention inside the multimodal diffusion transformers, enabling more precise semantic control. Extensive experiments on image reconstruction and text-guided editing tasks demonstrate that our method achieves state-of-the-art performance in terms of fidelity and editability. Code is available at https://github.com/wmchen/RKSovler_DDTA.

1 Introduction

Text-to-image diffusion models [13, 32, 37, 34, 1, 2, 28, 39, 5, 11] have achieved remarkable progress with powerful capabilities in generating diverse and realistic images conditioned on textual prompts. Recent research on Rectified Flow (RF) [22, 21, 11] models (*e.g.*, FLUX [20]) has demonstrated superior generative performance, surpassing previous DDIM-based [40, 8] methods such as Stable Diffusion (SD) [34, 28, 39].

The image generation process in diffusion models starts from an initial Gaussian noise and progressively denoises it to approximate the target data distribution. Consequently, a critical challenge in ensuring consistency lies in *how to invert a given image to a specific noise sample that can reconstruct it faithfully*. To date, only a limited number of studies [51, 35, 48, 6] have explored inversion for RF models. However, their performance remains significantly below the VQAE [34] upper bound, primarily due to the inherent sparsity of the RF latent space. This motivates the need for a higher-order inversion technique with a lower error bound tailored for RF models.

In text-guided image editing with diffusion models, the target prompt is applied during the denoising process. Therefore, another key challenge is *how to effectively leverage the source information from the inversion process to balance the trade-off between faithfulness and editability*. Existing approaches for RF models [48, 6, 42, 54] reuse the source attention features of query, key, and value from the inversion process to enhance the fidelity. However, state-of-the-art (SoTA) RF models adopt the Multimodal Diffusion Transformer (MM-DiT) architecture [27], which jointly encodes and processes both text and image modalities within a unified transformer framework. As a result, directly

*Corresponding author.

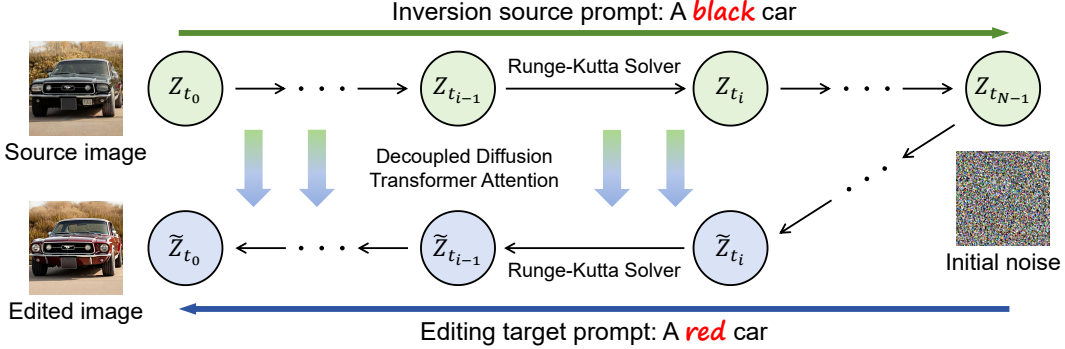


Figure 1: Conceptual illustration of our text-guided semantic editing framework.

reusing the attention features with entangled text and image information may lead to degradation in editing precision.

To address the first challenge, we propose an efficient high-order inversion method for rectified flow models based on the Runge-Kutta solver of differential equations. To tackle the second challenge, we introduce Decoupled Diffusion Transformer Attention (DDTA), a novel mechanism that disentangles text and image attention inside the multimodal diffusion transformers, enabling more precise semantic control. Extensive experiments on image reconstruction and text-guided editing tasks demonstrate that our method achieves state-of-the-art performance in terms of fidelity and editability.

As shown in Fig. 1, in this paper, we propose Runge-Kutta approximation and decoupled attention for RF inversion and semantic editing. Specifically, to address the first challenge, we incorporate the Runge-Kutta (RK) method from numerical analysis into the RF sampling process and propose a high-order solver for the differential process of RF. To tackle the second challenge, we delve into the internal structure of MM-DiT and decouple the tightly entangled text and image attention in MM-DiTs, thereby enabling more precise control over the semantic editability. To comprehensively evaluate the proposed method, we conduct extensive experiments on both image reconstruction and text-guided semantic editing tasks. Experimental results on the reconstruction task show that our RK solver improves inversion fidelity, achieving a PSNR (Peak Signal-to-Noise Ratio) gain up to 2.39 dB, which is quite significant. The results of the editing task demonstrate that our method achieves a superior overall performance in terms of fidelity and editability compared to SoTA RF-based methods.

2 Related Work and Unique Contributions

Our work is closely related to existing inversion methods and text-guided semantic editing. In this section, we first review existing work on these two related research areas. We then summarize the unique contributions of this work.

2.1 Inversion for Rectified Flow Models

Inversion serves as a fundamental building block for real-world image manipulation, which has been widely studied in SD literature [24, 9, 10, 25, 48, 35, 6, 8, 40, 46, 52, 47, 38]. However, due to the theoretical differences between DDIM and RF, these successful DDIM-based methods cannot be directly applied to RF-based models. RF-Prior [51] performs score distillation to invert a given image using RF models. However, this method incurs substantial computational overhead due to the large number of required optimization steps. RF inversion [35] improves the inversion quality by employing dynamic optimal control derived from linear quadratic regulators. However, it leverages information from the source image during the inversion process to enhance fidelity, which deviates from the notion of true inversion. RF-Solver [48] uses the Taylor expansion to reduce inversion errors in the ordinary differential equations (ODEs) of RF models. FireFlow [6] reuses intermediate velocity approximations to achieve the second-order accuracy while maintaining the computational cost of a first-order method. Unlike previous methods, this work employs the Runge-Kutta method to achieve a higher-order, training-free, and more accurate approximation of the differential process in RF.

2.2 Text-guided Semantic Editing with DiT-based models

Image editing aims to modify the visual content in a controllable manner while preserving the overall structure of the original image. Among various approaches, text-guided semantic editing has attracted the most research attention due to its remarkable flexibility [15]. Text-guided semantic editing based on diffusion models has been widely studied in recent years [18, 23, 12, 43, 24, 9, 3, 26, 17, 49, 25, 46, 14]. However, due to the significant structural differences between UNet-based (*e.g.*, SD) and DiT-based (*e.g.*, FLUX) models, these methods fail to apply to DiT-based models directly. RF-Solver [48] and FireFlow [6] replace the value attention feature of single-stream DiT blocks in the editing branch with those from the inversion branch to balance the faithfulness and editability. KV-Edit [54] caches the keys and values corresponding to the background during the inversion process and reuses them during the denoising to improve background consistency. However, it requires an additional mask input to separate the foreground from the background, making it less flexible than purely text-guided semantic editing. Add-it [42] utilizes both keys and values of DiT blocks from the source image to guide the editing process. However, its latent blending mechanism relies on SAM-2 [33] to obtain an object mask, introducing additional computational overhead. In contrast to previous methods, this work delves into the internal structure of MM-DiT and decouples the entangled text and image attention, thereby enabling precise text-guided semantic editing without introducing additional overhead.

2.3 Unique Contributions

Compared to existing methods, our unique contributions include: (1) We incorporate the Runge-Kutta method into the RF sampling process to perform high-order modeling of the differential trajectory, and propose a high-fidelity inversion method that better aligns the inversion and denoising paths. (2) We introduce a decoupled attention mechanism that decouples the entangled text and image attention in MM-DiTs, thereby enabling precise semantic editing in MM-DiT architectures. (3) Extensive experimental results on benchmark datasets demonstrate that our method achieves superior performance on both reconstruction and text-guided semantic editing tasks.

3 The Proposed Method

In this section, we first provide a brief overview of the relevant background knowledge and our method, followed by detailed descriptions of the proposed Runge-Kutta solver and DDTA.

3.1 Preliminaries and Method Overview

(1) Preliminaries. Rectified Flow (RF) [22] transits the standard Gaussian noise (source) distribution p_1 to the real data (target) distribution p_0 along a straight path. This transition is modeled by an ordinary differential equation (ODE) over a continuous time interval $t \in [0, 1]$:

$$dZ_t = v(Z_t, t) dt, \quad (1)$$

where $Z_0 \sim p_0$ denotes the image latent representation sampled from the target distribution, and $Z_1 \sim p_1$ is the noise latent sampled from the source distribution $\mathcal{N}(0, I)$. Given an initial state Z_0 and a terminal state Z_1 , the forward process (*i.e.*, adding noise) of RF follows a linear path defined as $Z_t = tZ_1 + (1 - t)Z_0$. This path induces a corresponding ODE: $dZ_t = (Z_1 - Z_0) dt$. Then, the training process employs a diffusion transformer v_θ , parameterized by θ , to approximate the ODE by solving the following least-squares regression objective:

$$\min_{\theta} \int_0^1 \mathbb{E} \left[\left\| \frac{dZ_t}{dt} - v_\theta(Z_t, t) \right\|_2^2 \right]. \quad (2)$$

In practice, the ODE is discretized and solved using the Euler method for the text-to-image RF models. Specifically, the RF process begins with a noise latent $Z_{t_N} \in \mathcal{N}(0, I)$, and performs denoising over N discrete timesteps $t = \{t_N, \dots, t_0\}$, progressively refining the latent representation until the final image latent Z_{t_0} is obtained:

$$Z_{t_{i-1}} = Z_{t_i} + (t_{i-1} - t_i) v_\theta(Z_{t_i}, t_i, \mathcal{P}), \quad (3)$$

where \mathcal{P} is the conditional prompt embedding extracted by the T5 text encoder [30].

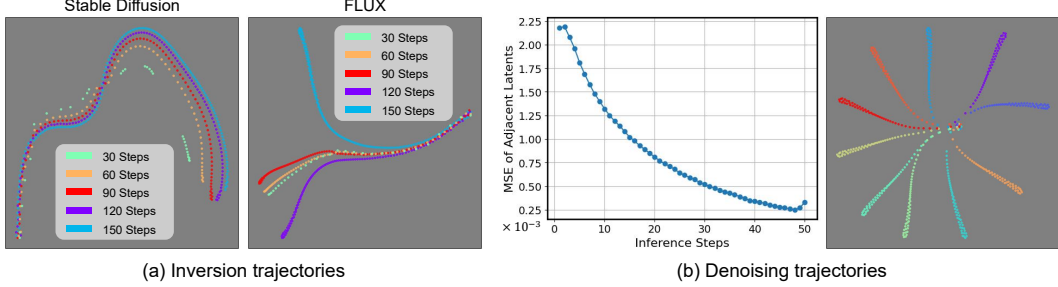


Figure 2: Visualization of the latent space. (a) Comparison of inversion trajectories between Stable Diffusion and FLUX. (b) Visualization of FLUX’s latent space, where the denoising processing is run for 50 steps from the same initial state using 10 different prompts.

(2) Method Overview. We identify two key challenges that lead to the imbalance between fidelity and editability in RF-based image inversion and semantic editing: (1) the sparsity of the RF latent space hinders accurate inversion, and (2) the entanglement of text and image modalities in MM-DiT’s limits precise control over attention features. To address these two tightly coupled challenges, we first incorporate the Runge-Kutta method with RF models and propose the RK Solver to perform high-order approximations of the differential process. Secondly, we propose the DDTA mechanism, which improves attention controllability by disentangling text and image modalities in MM-DiT’s, thereby achieving a better balance between fidelity and editability.

3.2 Runge-Kutta Solver for Rectified Flow Models

Despite the impressive image generation performance of the vanilla RF sampler, it suffers from severely degraded fidelity in inversion. For a more intuitive observation about the latent space manifold, we apply t-distributed stochastic neighbor embedding (t-SNE) [45] to project the high-dimensional latent representations onto a 2D plane, as illustrated in Fig. 2. As shown in Fig. 2 (a), we observe that the latent space of FLUX appears sparser than that of SD. Specifically, while the inversion trajectories of SD with varying steps follow similar trends, those of FLUX exhibit greater divergence. This suggests that FLUX explores more diverse latent directions during inversion, making it more difficult to achieve accurate reconstruction. To this end, it is necessary to introduce a higher-order ODE approximation to improve the reconstruction performance. In addition, as shown in Fig. 2 (b), the sampling process of FLUX is smooth. The smoothness of the learned ODE trajectory in FLUX arises from the linear interpolation in the forward process, making the system a non-stiff differential equation. Therefore, the well-studied explicit Runge-Kutta (RK) method from numerical analysis becomes a naturally suitable high-order solver for the ODE in RF.

We now present the inversion form of the proposed RK solver. Given a known state at the $(i - 1)$ -th timestep $Z_{t_{i-1}}$, an r -order of explicit RK solver builds a series of intermediate slopes $\{K_1^i, \dots, K_r^i\}$:

$$K_s^i = v_\theta \left(Z_{t_{i-1}} + \Delta t_i \sum_{j=1}^{s-1} a_{sj} K_j^i, t_{i-1} + c_s \Delta t_i, \mathcal{P} \right), \quad (4)$$

where $\Delta t_i = t_i - t_{i-1}$ denotes the step size of adjacent states. Then, the next state Z_{t_i} can be computed by:

$$Z_{t_i} = Z_{t_{i-1}} + \Delta t_i \sum_{j=1}^r b_j K_j^i. \quad (5)$$

Note that the lower triangular matrix $\mathbf{A} = [a_{mn}]$ together with the vectors \mathbf{b}^T and \mathbf{c} , constitute a Butcher tableau, *i.e.*,

$$\mathbf{B} = \begin{array}{c|c} \mathbf{c} & \mathbf{A} \\ \hline & \mathbf{b}^T \end{array}. \quad (6)$$

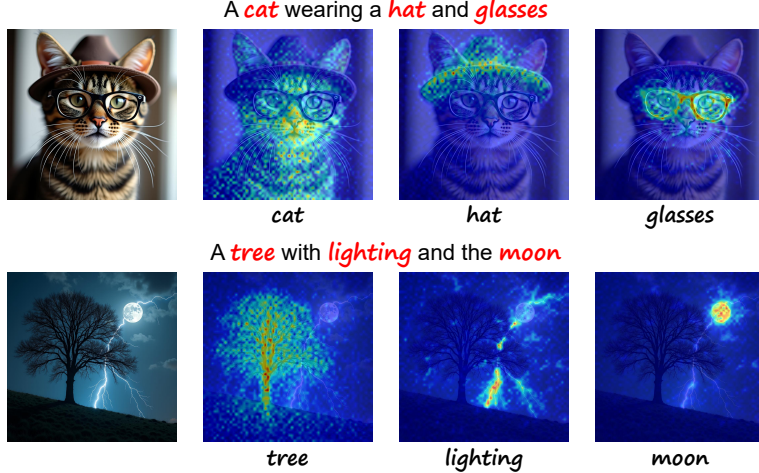


Figure 3: Visualization of the response maps corresponding to the decoupled cross-attention components. We aggregate cross-attention maps across all DiT blocks during the sampling process to show the spatial correlation between image layout and prompt words. The details of the visualization are provided in the appendix.

The denoising process of the RK solver has a symmetrical formulation, *i.e.*,

$$K_s^i = v_\theta \left(Z_{t_i} - \Delta t_i \sum_{j=1}^{s-1} a_{sj} K_j^i, t_i - c_s \Delta t_i, \mathcal{P} \right), \quad (7)$$

$$Z_{t_{i-1}} = Z_{t_i} - \Delta t_i \sum_{j=1}^r b_j K_j^i. \quad (8)$$

Empirically, the RK solver should adopt the same order for both the inversion and denoising processes. The complete inversion process with our RK solver is provided in pseudocode in the Appendix.

Noting that the existing inversion methods, RF-Solver and FireFlow, can be regarded as two specific variants of our RK solver. RF-Solver uses the Taylor expansion to approximate the velocity prediction, while FireFlow uses the midpoint method. Thus, their Butcher tableaus are given by:

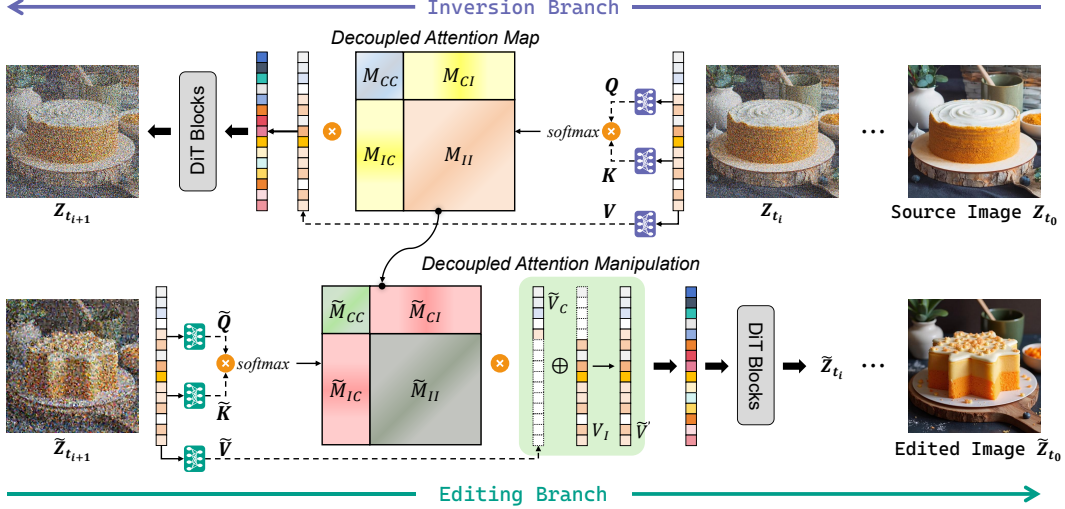
$$\mathbf{B}_{\text{RF-Solver}} = \begin{array}{c|cc} 0 & 0 & 0 \\ \frac{1}{2} & \frac{1}{2} & 0 \\ \frac{3}{4} & \frac{1}{4} & \end{array}, \quad \mathbf{B}_{\text{FireFlow}} = \begin{array}{c|cc} 0 & 0 & 0 \\ \frac{1}{2} & \frac{1}{2} & 0 \\ 0 & 1 & \end{array}. \quad (9)$$

In addition, FireFlow achieves runtime acceleration by reusing the midpoint velocity from the previous step to approximate the current velocity, *i.e.*, $K_1^i \approx K_2^{i-1}$.

3.3 Decoupled Diffusion Transformer Attention for Semantic Image Editing

Text-guided semantic editing attracts the most attention due to its flexibility. Representative methods (*e.g.*, P2P [12]) focus on manipulating attentions in the editing branch by leveraging the preserved attentions from the inversion branch. The effectiveness of these methods stems from the separate design of self-attention and cross-attention mechanisms in UNet-based diffusion models. However, the MM-DiT-based diffusion models process text and image information jointly within a unified transformer framework, making it difficult to transfer those effective methods to DiT-based architectures. Specifically, the MM-DiT architecture consists of two types of transformer blocks, *i.e.*, multi-stream and single-stream DiT blocks. In the multi-stream DiT block, text and image attention features are first extracted separately:

$$\mathcal{F}_C^l = W_{\mathcal{F}_C}^l (h_C^l), \quad \mathcal{F}_I^l(t_i) = W_{\mathcal{F}_I}^l (h_I^l(t_i)). \quad (10)$$



Prompt: a *round star* cake with orange frosting on a wooden plate

Figure 4: Overview of Decoupled Diffusion Transformer Attention (DDTA)

Here, l denotes the layer index of the DiT block. $W(\cdot)$ represents the pre-trained attention projection in the transformer. $\mathcal{F}_C = \{Q_C, K_C, V_C\}$ is the attention feature corresponding to the conditional hidden state related to the textual prompt, while $\mathcal{F}_I(t_i) = \{Q_I(t_i), K_I(t_i), V_I(t_i)\}$ correspond to the attention feature derived from the hidden state associated with the image latent at timestep t_i . Then, attention features are concatenated $\mathcal{F}^l = \mathcal{F}_C^l \oplus \mathcal{F}_I^l(t_i)$, followed by the attention computation:

$$\text{Attention}(Q, K, V) = \text{softmax}\left(\frac{QK^T}{\sqrt{d}}\right) \cdot V. \quad (11)$$

In the single-stream DiT block, text and image hidden states are concatenated before attention feature extraction, *i.e.*,

$$\mathcal{F}^l(t_i) = W_{\mathcal{F}}^l(h_C^l \oplus h_I^l(t_i)). \quad (12)$$

According to the observation of the internal structure, the attention map of the DiT block can be decoupled into four regions based on the dimension of hidden states:

$$M = \text{softmax}\left(\frac{QK^T}{\sqrt{d}}\right) = \left[\begin{array}{c|c} M_{CC} & M_{CI} \\ \hline M_{IC} & M_{II} \end{array} \right], \quad (13)$$

where M_{CC} and M_{II} correspond to the self-attention maps of the condition and image, while M_{CI} and M_{IC} represent the cross-attention maps between condition and image. As shown in Fig. 3, the decoupled cross-attention maps reveal strong spatial correlations between image layout and prompt words, demonstrating the effectiveness of our attention decoupling method. In addition, the value feature can also be decoupled into two regions according to the dimension: $V = [V_C|V_I]$.

Therefore, the proposed attention decoupling mechanism facilitates effective text-guided semantic editing via fine-grained attention manipulation. Specifically, as illustrated in Fig. 4, attentions in the editing branch $\tilde{M} = \{\tilde{M}_{CC}, \tilde{M}_{CI}, \tilde{M}_{IC}, \tilde{M}_{II}, \tilde{V}\}$ are modified based on the preserved attentions in the inversion branch $M = \{M_{CC}, M_{CI}, M_{IC}, M_{II}, V\}$. We consider two types of operations, *i.e.*,

$$\text{Replacement: } \tilde{M}' = M, \quad \text{Mean: } \tilde{M}' = (M + \tilde{M})/2. \quad (14)$$

Both operations improve the faithfulness of the edited image, with the replacement strategy yielding a greater fidelity gain than the mean operation. This indicates that preserving original attention features is more effective in maintaining content consistency. Moreover, incorporating a larger proportion of attention features into the manipulation enhances fidelity to the source image but reduces editability. These findings highlight the inherent trade-off between fidelity and editability,

Table 1: Comparison results on the reconstruction task. The best result for each metric is highlighted in bold, and the second-best is underlined (excluding the VQAE method).

Method	PSNR \uparrow	SSIM \uparrow	LPIPS \downarrow
VQAE (upper bound)	32.95	0.9347	0.0121
Vanilla RF	17.46	0.5952	0.4282
RF Inversion [35]	22.14	0.6540	<u>0.1388</u>
RF-Solver [48]	22.20	0.7778	0.1890
Fireflow [6]	23.29	0.8006	0.1639
Ours ($r = 2$)	<u>24.00</u>	0.8124	0.1534
Ours ($r = 3$)	23.98	<u>0.8131</u>	0.1497
Ours ($r = 4$)	25.68	0.8364	0.1241

which must be carefully balanced in image editing tasks. For general semantic editing purposes, applying the replacement operation to cross-attention maps $\{\widetilde{M}_{C\mathcal{I}}, \widetilde{M}_{\mathcal{I}C}\}$ and the mean operation to the image region of value attention feature $\widetilde{V}_{\mathcal{I}}$ in single-stream DiT blocks is typically sufficient. Furthermore, users can flexibly customize both the manipulation type as well as the number of blocks or sampling steps to achieve the most satisfactory result for a given image.

4 Experimental Results

In this section, we conduct comprehensive evaluations of the proposed method and provide detailed ablation studies to further understand its performance. Additional results are provided in the Supplemental Materials.

4.1 Experiment Settings

Baselines. We adopt FLUX.1-dev with the vanilla RF Euler sampler as the baseline for all tasks. For the reconstruction task, we compare SoTA inversion approaches designed for RF models, such as RF inversion [35], RF-Solver [48], and FireFlow [6]. For the editing task, we include both RF-based methods and DDIM-based approaches for comparison. Here, the DDIM-based methods include P2P [12], MasaCtrl [4], and PnP [43].

Datasets and Evaluation Metrics. We evaluate the proposed method on two tasks: image reconstruction and text-guided semantic editing. To comprehensively assess the reconstruction performance of our RK solver, we report results on the first 1,000 images from the Densely Captioned Images (DCI) dataset [44], using Peak Signal-to-Noise Ratio (PSNR), Structural Similarity Index Measure (SSIM) [50], and Learned Perceptual Image Patch Similarity (LPIPS) [53] as evaluation metrics. For the editing task, we assess our framework on the PIE-Bench dataset [16]. We use CLIP [29] to measure the alignment between the edited image and the guiding text. To evaluate the fidelity of non-edited regions, we further report PSNR, SSIM, and structural distance [16].

Implementation Details. All methods are implemented by PyTorch and the Diffusers library, and all reported results are based on our re-implementation. Stable Diffusion v1.5 serves as the baseline model for all DDIM-based methods. Images from the DCI dataset are center-cropped to square format and resized to 1024×1024 , using the short version of the provided captions. For RF-based methods, the guidance scales for the inversion and editing branches are set to 1.0 and 3.0, respectively. The configuration of our DDTA follows the general setup described in Sec. 3.3, with attention manipulation applied only to the single-stream DiT blocks at the first sampling step. All experiments are conducted on a single NVIDIA A100-80G SXM GPU.

4.2 Image Reconstruction Task

We compare our proposed RK solver against VQAE, vanilla RF, RF inversion, RF-Solver, and FireFlow. The VQAE method represents the upper bound of reconstruction performance, as it directly decodes the image latent Z_{t_0} obtained from the encoder. Notably, RF inversion reuses the image latent from the inversion process during denoising, and thus does not perform a real inversion.

Table 2: Comparison results on the text-guided semantic editing task. The best result for each metric is highlighted in bold, and the second-best is underlined.

Method	Baseline	Structure Distance↓	Unedited PSNR↑	Fidelity SSIM↑	CLIP Similarity Whole↑	CLIP Similarity Edited↑	Steps
P2P [12]	SD	0.0699	17.84	0.7141	25.18	22.35	50
MasaCtrl [4]	SD	0.0277	22.31	0.8041	23.99	21.15	50
PnP [43]	SD	0.0273	22.32	0.7958	25.42	<u>22.52</u>	50
RF Inversion [35]	FLUX	0.0446	20.31	0.7014	25.07	22.36	28
RF-Solver [48]	FLUX	0.0297	22.27	0.7938	24.61	21.87	25
FireFlow [6]	FLUX	<u>0.0264</u>	23.30	0.8302	24.53	21.65	8
Ours ($r = 2$)	FLUX	0.0288	23.29	0.8296	<u>25.30</u>	22.54	8
Ours ($r = 3$)	FLUX	0.0284	23.51	0.8339	<u>25.30</u>	22.50	8
Ours ($r = 4$)	FLUX	0.0259	24.24	0.8535	24.67	21.95	8
Ours ($r = 4$)	FLUX	0.0271	<u>23.76</u>	<u>0.8431</u>	25.26	22.48	5

Table 3: User study of the text-guided semantic editing task on the PIE-Bench dataset.

Method	Qwen-VL-Max	Hunyuan-T1	Doubao-1.5
P2P [12]	4.01	10.74	6.59
MasaCtrl [4]	14.59	9.31	7.74
PnP [43]	15.74	14.18	17.34
RF Inversion [35]	12.59	10.89	7.88
RF-Solver [48]	11.59	13.75	6.03
FireFlow [6]	8.44	15.75	10.32
Ours	33.04	25.36	44.13

The comparison of RF inversion is solely for the completeness of the experiment. The results are presented in Tab. 1, demonstrating that our method outperforms all existing approaches across all evaluation metrics. We report the results based on the best-performing configurations, using Heun’s second-order, Kutta’s third-order, and the 3/8-rule fourth-order [19] variants, whose corresponding Butcher tableaus are as follows:

$$\mathbf{B}_{r=2} = \begin{array}{c|cc} 0 & 0 & 0 \\ 1 & 1 & 0 \\ \hline & \frac{1}{2} & \frac{1}{2} \end{array}, \quad \mathbf{B}_{r=3} = \begin{array}{c|ccc} 0 & 0 & 0 & 0 \\ \frac{1}{2} & \frac{1}{2} & 0 & 0 \\ 1 & -1 & 2 & 0 \\ \hline & \frac{1}{6} & \frac{2}{3} & \frac{1}{6} \end{array}, \quad \mathbf{B}_{r=4} = \begin{array}{c|cccc} 0 & 0 & 0 & 0 & 0 \\ \frac{1}{3} & \frac{1}{3} & 0 & 0 & 0 \\ \frac{2}{3} & -\frac{1}{3} & 1 & 0 & 0 \\ 1 & 1 & -1 & 1 & 0 \\ \hline & \frac{1}{8} & \frac{3}{8} & \frac{3}{8} & \frac{1}{8} \end{array}.$$

The third-order variant slightly outperforms the second-order one, while our fourth-order variant achieves the best reconstruction performance, surpassing FireFlow by 10.3%, 4.5%, and 24.3% in PSNR, SSIM, and LPIPS, respectively.

4.3 Text-Guided Semantic Editing Task

Quantitative Results. We conduct a comprehensive quantitative comparison on the PIE-bench dataset across various methods, including both DDIM-based and RF-based methods, using SDv1.5 and FLUX.1-dev as their respective baselines. Noting that the results of our method presented in this section are achieved through the combination of the proposed RK Solver and DDTA. Quantitative results shown in Tab. 2 support the following three conclusions: (1) Our method outperforms all baselines in content consistency, with our fourth-order variant achieving the highest PSNR, SSIM, and structure distance. (2) Our method demonstrates competitive editability (closely trailing the best result) while maintaining substantially higher fidelity, highlighting a more favorable trade-off between fidelity and editability. (3) Our method achieves the best overall performance with significantly fewer sampling steps, indicating the superior efficiency of our method.

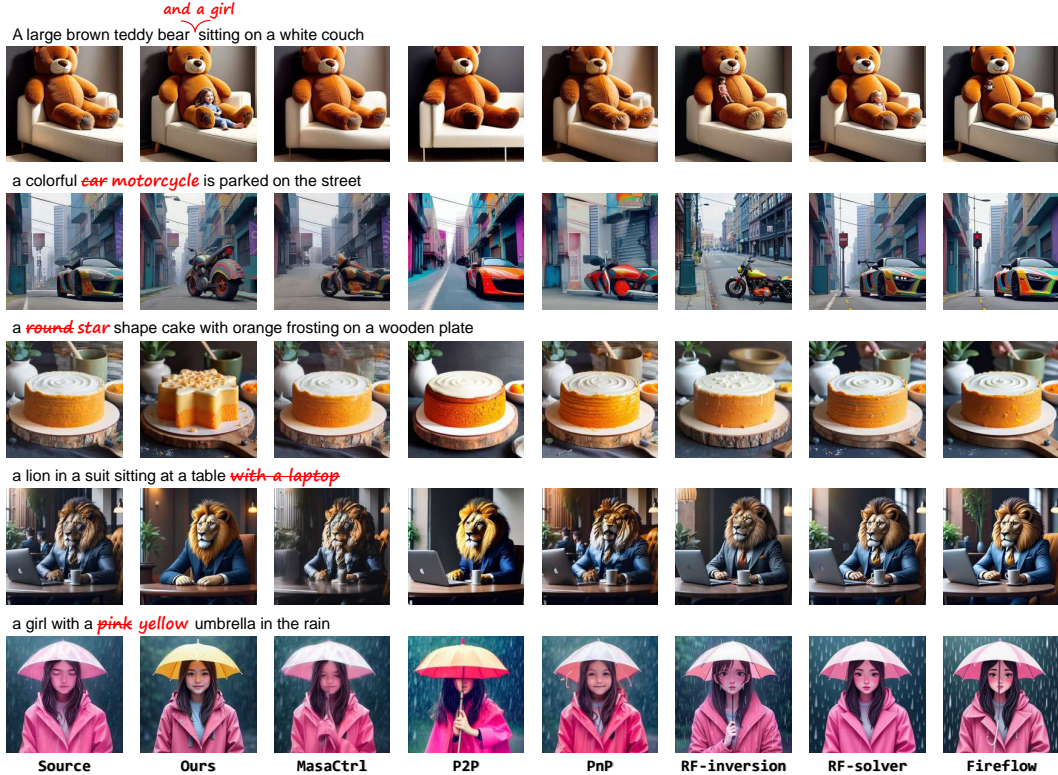


Figure 5: Qualitative results on the text-guided semantic editing task.

Table 4: Ablation study on the trade-off between fidelity and editability.

RK Solver	DDTA	Structure Distance↓	Unedited PSNR↑	Fidelity SSIM↑	CLIP Similarity Whole↑	Edited↑
✗	✗	0.0264	23.30	0.8302	24.53	21.65
✓	✗	0.0133	28.42	0.8918	23.74	21.00
✗	✓	0.0358	22.18	0.8177	25.73	22.99
✓	✓	0.0284	23.51	0.8339	25.30	22.50

Qualitative Results. As shown in Fig. 5, we present qualitative results demonstrating the effectiveness of our method across diverse editing types, including both object and attribute manipulations. While minor unintended background changes may occur, our method consistently outperforms existing baselines in terms of semantic alignment with target prompts and structural consistency with source images, highlighting its robustness and versatility in the text-guided semantic editing task.

User Study. To further evaluate the effectiveness of our proposed method, we employ Multimodal Large Language Models (MLLMs) to assess the quality of edited images based on both editing performance and consistency with the source image. To ensure the reliability of the evaluation, we select three state-of-the-art MLLMs as independent judges: Qwen-VL-Max, Hunyuan-T1, and Doubao-1.5. This evaluation is performed on the entire PIE-Bench dataset, where for each image, the MLLMs are tasked with selecting the best-edited result among all compared methods. In this study, we adopt the fourth-order variant with 5 sampling steps for comparison against other baselines. We report the proportion of selections for each method across the dataset. As shown in Tab. 3, our proposed method is selected significantly more often than all comparisons, demonstrating its superior editing quality and faithfulness.

4.4 Ablation Studies

To assess the contribution of each component in our framework, we perform an ablation study on the PIE-Bench dataset. We use FireFlow as the baseline and compare it against our third-order variant under a fixed setting of 8 sampling steps. As shown in Tab. 4, our full framework, which integrates the proposed RK Solver and DDTA, achieves the best balance between fidelity and editability. Specifically, replacing the baseline sampler with the RK Solver significantly improves content consistency, though the alignment with the editing prompt remains limited. In contrast, substituting the editing module with DDTA leads to substantial gains in editability, but at the cost of significantly reduced fidelity. Additional ablation studies are provided in the Appendix, including the selection of the Butcher tableau, the contribution of each sub-attention feature, and the effectiveness of different attention manipulation strategies.

5 Conclusion

In this work, we address two critical limitations of applying RF models to real-world image editing: the difficulty of accurate inversion due to latent space sparsity and the lack of semantic controllability stemming from entangled multimodal attention. To overcome the first challenge, we propose RK Solver, a high-order inversion technique inspired by the well-studied Runge-Kutta method from numerical analysis. To address the second challenge, we introduce DDTA, a novel attention mechanism that decouples text and image modalities in MM-DiT. Extensive experimental results on image reconstruction and text-guided editing tasks demonstrate the effectiveness of our approach, which achieves the SoTA performance in terms of fidelity and editability. Regarding the societal impact of this work, our method not only enhances the practical applicability of RF models in real-world generative tasks but also provides new insights into controllable diffusion-based generation. These advancements have the potential to benefit various domains, including the creative industries, digital art, education, and accessibility. Although the proposed RK solver significantly improves fidelity, its high-order modeling introduces additional computational overhead. Additionally, preserving the decoupled attention maps incurs notable memory consumption. These limitations suggest promising directions for future work, including the development of high-order solvers with low computational overhead and the design of efficient attention-preserving mechanisms, which could further improve the practicality of RF models.

Acknowledgments

This work is supported by the National Natural Science Foundation of China (No. 62331014) and Project 2021JC02X103. We acknowledge the computational support of the Center for Computational Science and Engineering at Southern University of Science and Technology.

References

- [1] Yogesh Balaji, Seungjun Nah, Xun Huang, Arash Vahdat, Jiaming Song, Qinsheng Zhang, Karsten Kreis, Miika Aittala, Timo Aila, Samuli Laine, Bryan Catanzaro, Tero Karras, and Ming-Yu Liu. ediff-i: Text-to-image diffusion models with an ensemble of expert denoisers, 2023.
- [2] James Betker, Gabriel Goh, Li Jing, Tim Brooks, Jianfeng Wang, Linjie Li, Long Ouyang, Juntang Zhuang, Joyce Lee, Yufei Guo, Wesam Manassra, Prafulla Dhariwal, Casey Chu, and Yunxin Jiao. Improving image generation with better captions. <https://cdn.openai.com/papers/dall-e-3.pdf>, 2023.
- [3] Tim Brooks, Aleksander Holynski, and Alexei A. Efros. Instructpix2pix: Learning to follow image editing instructions. In *2023 IEEE/CVF Conference on Computer Vision and Pattern Recognition (CVPR)*, pages 18392–18402, 2023.
- [4] Mingdeng Cao, Xintao Wang, Zhongang Qi, Ying Shan, Xiaohu Qie, and Yinqiang Zheng. Masactrl: Tuning-free mutual self-attention control for consistent image synthesis and editing. In *2023 IEEE/CVF International Conference on Computer Vision (ICCV)*, pages 22503–22513, 2023.

- [5] Junsong Chen, Jincheng YU, Chongjian GE, Lewei Yao, Enze Xie, Zhongdao Wang, James Kwok, Ping Luo, Huchuan Lu, and Zhenguo Li. Pixart- α : Fast training of diffusion transformer for photorealistic text-to-image synthesis. In *The Twelfth International Conference on Learning Representations*, 2024.
- [6] Yingying Deng, Xiangyu He, Changwang Mei, Peisong Wang, and Fan Tang. Fireflow: Fast inversion of rectified flow for image semantic editing. In *Forty-second International Conference on Machine Learning*, 2025.
- [7] Van der Houwen P J. Explicit runge-kutta formulas with increased stability boundaries. *Numerische Mathematik*, 20:149–164, 1972.
- [8] Prafulla Dhariwal and Alexander Nichol. Diffusion models beat gans on image synthesis. In *Advances in Neural Information Processing Systems*, volume 34, pages 8780–8794. Curran Associates, Inc., 2021.
- [9] Wenkai Dong, Song Xue, Xiaoyue Duan, and Shumin Han. Prompt tuning inversion for text-driven image editing using diffusion models. In *2023 IEEE/CVF International Conference on Computer Vision (ICCV)*, pages 7396–7406, 2023.
- [10] Xiaoyue Duan, Shuhao Cui, Guoliang Kang, Baochang Zhang, Zhengcong Fei, Mingyuan Fan, and Junshi Huang. Tuning-free inversion-enhanced control for consistent image editing. *Proceedings of the AAAI Conference on Artificial Intelligence*, 38(2):1644–1652, Mar. 2024.
- [11] Patrick Esser, Sumith Kulal, Andreas Blattmann, Rahim Entezari, Jonas Müller, Harry Saini, Yam Levi, Dominik Lorenz, Axel Sauer, Frederic Boesel, Dustin Podell, Tim Dockhorn, Zion English, and Robin Rombach. Scaling rectified flow transformers for high-resolution image synthesis. ICML’24. JMLR.org, 2024.
- [12] Amir Hertz, Ron Mokady, Jay Tenenbaum, Kfir Aberman, Yael Pritch, and Daniel Cohen-or. Prompt-to-prompt image editing with cross-attention control. In *The Eleventh International Conference on Learning Representations*, 2023.
- [13] Jonathan Ho, Ajay Jain, and Pieter Abbeel. Denoising diffusion probabilistic models. In *Advances in Neural Information Processing Systems*, volume 33, pages 6840–6851. Curran Associates, Inc., 2020.
- [14] Jiancheng Huang, Yifan Liu, Jin Qin, and Shifeng Chen. Kv inversion: Kv embeddings learning for text-conditioned real image action editing. In *Pattern Recognition and Computer Vision*, pages 172–184, Singapore, 2024. Springer Nature Singapore.
- [15] Yi Huang, Jiancheng Huang, Yifan Liu, Mingfu Yan, Jiayi Lv, Jianzhuang Liu, Wei Xiong, He Zhang, Liangliang Cao, and Shifeng Chen. Diffusion model-based image editing: A survey. *IEEE Transactions on Pattern Analysis and Machine Intelligence*, pages 1–27, 2025.
- [16] Xuan Ju, Ailing Zeng, Yuxuan Bian, Shaoteng Liu, and Qiang Xu. Pnp inversion: Boosting diffusion-based editing with 3 lines of code. In *The Twelfth International Conference on Learning Representations*, 2024.
- [17] Bahjat Kawar, Shiran Zada, Oran Lang, Omer Tov, Huiwen Chang, Tali Dekel, Inbar Mosseri, and Michal Irani. Imagic: Text-based real image editing with diffusion models. In *2023 IEEE/CVF Conference on Computer Vision and Pattern Recognition (CVPR)*, pages 6007–6017, 2023.
- [18] Gwanghyun Kim, Taesung Kwon, and Jong Chul Ye. Diffusionclip: Text-guided diffusion models for robust image manipulation. In *2022 IEEE/CVF Conference on Computer Vision and Pattern Recognition (CVPR)*, pages 2416–2425, 2022.
- [19] W. Kutta. Beitrag zur näherungsweise Integration totaler Differentialgleichungen. *Zeit. Math. Phys.*, 46:435–53, 1901.
- [20] Black Forest Labs. Flux. <https://github.com/black-forest-labs/flux>, 2024.

- [21] Yaron Lipman, Ricky T. Q. Chen, Heli Ben-Hamu, Maximilian Nickel, and Matthew Le. Flow matching for generative modeling. In *The Eleventh International Conference on Learning Representations*, 2023.
- [22] Xingchao Liu, Chengyue Gong, and Qiang Liu. Flow straight and fast: Learning to generate and transfer data with rectified flow. In *The Eleventh International Conference on Learning Representations*, 2023.
- [23] Daiki Miyake, Akihiro Iohara, Yu Saito, and Toshiyuki Tanaka. Negative-prompt inversion: Fast image inversion for editing with text-guided diffusion models, 2023.
- [24] Ron Mokady, Amir Hertz, Kfir Aberman, Yael Pritch, and Daniel Cohen-Or. Null-text inversion for editing real images using guided diffusion models. In *2023 IEEE/CVF Conference on Computer Vision and Pattern Recognition (CVPR)*, pages 6038–6047, 2023.
- [25] Zhihong Pan, Riccardo Gherardi, Xiufeng Xie, and Stephen Huang. Effective real image editing with accelerated iterative diffusion inversion. In *2023 IEEE/CVF International Conference on Computer Vision (ICCV)*, pages 15866–15875, 2023.
- [26] Gaurav Parmar, Krishna Kumar Singh, Richard Zhang, Yijun Li, Jingwan Lu, and Jun-Yan Zhu. Zero-shot image-to-image translation. In *ACM SIGGRAPH 2023 Conference Proceedings, SIGGRAPH '23*, New York, NY, USA, 2023. Association for Computing Machinery.
- [27] William Peebles and Saining Xie. Scalable diffusion models with transformers. In *Proceedings of the IEEE/CVF international conference on computer vision*, pages 4195–4205, 2023.
- [28] Dustin Podell, Zion English, Kyle Lacey, Andreas Blattmann, Tim Dockhorn, Jonas Müller, Joe Penna, and Robin Rombach. SDXL: Improving latent diffusion models for high-resolution image synthesis. In *The Twelfth International Conference on Learning Representations*, 2024.
- [29] Alec Radford, Jong Wook Kim, Chris Hallacy, Aditya Ramesh, Gabriel Goh, Sandhini Agarwal, Girish Sastry, Amanda Askell, Pamela Mishkin, Jack Clark, Gretchen Krueger, and Ilya Sutskever. Learning transferable visual models from natural language supervision. In *Proceedings of the 38th International Conference on Machine Learning*, volume 139 of *Proceedings of Machine Learning Research*, pages 8748–8763. PMLR, 18–24 Jul 2021.
- [30] Colin Raffel, Noam Shazeer, Adam Roberts, Katherine Lee, Sharan Narang, Michael Matena, Yanqi Zhou, Wei Li, and Peter J. Liu. Exploring the limits of transfer learning with a unified text-to-text transformer. *Journal of Machine Learning Research*, 21(140):1–67, 2020.
- [31] Anthony Ralston. Runge-kutta methods with minimum error bounds. *Mathematics of Computation*, 16(80):431–437, 1962.
- [32] Aditya Ramesh, Prafulla Dhariwal, Alex Nichol, Casey Chu, and Mark Chen. Hierarchical text-conditional image generation with clip latents, 2022.
- [33] Nikhila Ravi, Valentin Gabeur, Yuan-Ting Hu, Ronghang Hu, Chaitanya Ryali, Tengyu Ma, Haitham Khedr, Roman Rädle, Chloe Rolland, Laura Gustafson, Eric Mintun, Junting Pan, Kalyan Vasudev Alwala, Nicolas Carion, Chao-Yuan Wu, Ross Girshick, Piotr Dollar, and Christoph Feichtenhofer. SAM 2: Segment anything in images and videos. In *The Thirteenth International Conference on Learning Representations*, 2025.
- [34] Robin Rombach, Andreas Blattmann, Dominik Lorenz, Patrick Esser, and Björn Ommer. High-resolution image synthesis with latent diffusion models. In *Proceedings of the IEEE/CVF Conference on Computer Vision and Pattern Recognition (CVPR)*, pages 10684–10695, June 2022.
- [35] Litu Rout, Yujia Chen, Nataniel Ruiz, Constantine Caramanis, Sanjay Shakkottai, and Wen-Sheng Chu. Semantic image inversion and editing using rectified stochastic differential equations. In *The Thirteenth International Conference on Learning Representations*, 2025.
- [36] Carl Runge. Über die numerische auflösung von differentialgleichungen. *Mathematische Annalen*, 46(2):167–178, 1895.

- [37] Chitwan Saharia, William Chan, Saurabh Saxena, Lala Li, Jay Whang, Emily L Denton, Kamyar Ghasemipour, Raphael Gontijo Lopes, Burcu Karagol Ayan, Tim Salimans, Jonathan Ho, David J Fleet, and Mohammad Norouzi. Photorealistic text-to-image diffusion models with deep language understanding. In *Advances in Neural Information Processing Systems*, volume 35, pages 36479–36494. Curran Associates, Inc., 2022.
- [38] Dvir Samuel, Barak Meiri, Haggai Maron, Yoav Tewel, Nir Darshan, Shai Avidan, Gal Chechik, and Rami Ben-Ari. Lightning-fast image inversion and editing for text-to-image diffusion models. In *The Thirteenth International Conference on Learning Representations*, 2025.
- [39] Axel Sauer, Dominik Lorenz, Andreas Blattmann, and Robin Rombach. Adversarial diffusion distillation. In *Computer Vision – ECCV 2024*, pages 87–103, Cham, 2024. Springer Nature Switzerland.
- [40] Jiaming Song, Chenlin Meng, and Stefano Ermon. Denoising diffusion implicit models. In *International Conference on Learning Representations*, 2021.
- [41] Raphael Tang, Linqing Liu, Akshat Pandey, Zhiying Jiang, Gefei Yang, Karun Kumar, Pontus Stenetorp, Jimmy Lin, and Ferhan Ture. What the DAAM: Interpreting stable diffusion using cross attention. In *Proceedings of the 61st Annual Meeting of the Association for Computational Linguistics (Volume 1: Long Papers)*, pages 5644–5659, Toronto, Canada, July 2023. Association for Computational Linguistics.
- [42] Yoav Tewel, Rinon Gal, Dvir Samuel, Yuval Atzmon, Lior Wolf, and Gal Chechik. Add-it: Training-free object insertion in images with pretrained diffusion models. In *The Thirteenth International Conference on Learning Representations*, 2025.
- [43] Narek Tumanyan, Michal Geyer, Shai Bagon, and Tali Dekel. Plug-and-play diffusion features for text-driven image-to-image translation. In *2023 IEEE/CVF Conference on Computer Vision and Pattern Recognition (CVPR)*, pages 1921–1930, 2023.
- [44] Jack Urbanek, Florian Bordes, Pietro Astolfi, Mary Williamson, Vasu Sharma, and Adriana Romero-Soriano. A picture is worth more than 77 text tokens: Evaluating clip-style models on dense captions. In *2024 IEEE/CVF Conference on Computer Vision and Pattern Recognition (CVPR)*, pages 26690–26699, 2024.
- [45] Laurens van der Maaten and Geoffrey Hinton. Visualizing data using t-sne. *Journal of Machine Learning Research*, 9(86):2579–2605, 2008.
- [46] Bram Wallace, Akash Gokul, and Nikhil Naik. Edict: Exact diffusion inversion via coupled transformations. In *2023 IEEE/CVF Conference on Computer Vision and Pattern Recognition (CVPR)*, pages 22532–22541, 2023.
- [47] Fangyikang Wang, Hubery Yin, Yuejiang Dong, Huminhao Zhu, Chao Zhang, Hanbin Zhao, Hui Qian, and Chen Li. Belm: Bidirectional explicit linear multi-step sampler for exact inversion in diffusion models. In *Advances in Neural Information Processing Systems*, volume 37, pages 46118–46159. Curran Associates, Inc., 2024.
- [48] Jiangshan Wang, Junfu Pu, Zhongang Qi, Jiayi Guo, Yue Ma, Nisha Huang, Yuxin Chen, Xiu Li, and Ying Shan. Taming rectified flow for inversion and editing. In *Forty-second International Conference on Machine Learning*, 2025.
- [49] kai Wang, Fei Yang, Shiqi Yang, Muhammad Atif Butt, and Joost van de Weijer. Dynamic prompt learning: Addressing cross-attention leakage for text-based image editing. In *Advances in Neural Information Processing Systems*, volume 36, pages 26291–26303. Curran Associates, Inc., 2023.
- [50] Zhou Wang, A.C. Bovik, H.R. Sheikh, and E.P. Simoncelli. Image quality assessment: from error visibility to structural similarity. *IEEE Transactions on Image Processing*, 13(4):600–612, 2004.
- [51] Xiaofeng Yang, Chen Cheng, Xulei Yang, Fayao Liu, and Guosheng Lin. Text-to-image rectified flow as plug-and-play priors. In *The Thirteenth International Conference on Learning Representations*, 2025.

- [52] Guoqiang Zhang, J. P. Lewis, and W. Bastiaan Kleijn. Exact diffusion inversion via bidirectional integration approximation. In *Computer Vision – ECCV 2024*, pages 19–36, Cham, 2024. Springer Nature Switzerland.
- [53] Richard Zhang, Phillip Isola, Alexei A. Efros, Eli Shechtman, and Oliver Wang. The unreasonable effectiveness of deep features as a perceptual metric. In *2018 IEEE/CVF Conference on Computer Vision and Pattern Recognition*, pages 586–595, 2018.
- [54] Tianrui Zhu, Shiyi Zhang, Jiawei Shao, and Yansong Tang. Kv-edit: Training-free image editing for precise background preservation, 2025.

Appendix

A Theoretical Analysis

In practice, v_θ is predicted by a neural network without a rigorous mathematical explicit expression. It may be unable to be exactly equal to the original required v for various reasons, including the performance of the neural network and the noise. This error could accumulate when finding the solution to the ODE by iterative methods. Therefore, understanding the bounds of this error is crucial for assessing and improving the denoising algorithm of flow matching. In this section, we will prove that this error has an upper bound as

$$|\tilde{Z}_{t_0} - Z_{t_0}| \leq e^\Lambda |\delta_0| + \frac{e^\Lambda - 1}{\Lambda} \max_{1 \leq i \leq N} |\delta_i|, \quad (15)$$

where \tilde{Z}_{t_0} is the ODE solution with perturbation, Z_{t_0} is the ODE solution by iterative method without any perturbation ideally, $\delta_i (i = 0, 1, 2, \dots, N)$ is the perturbation at step i , and $\Lambda = (41/24)L$ (L is Lipschitz constant).

Proof. The process of solving ODE is determining Z_{t_0} based on the given Z_{t_N} . This can be achieved using the general Runge-Kutta method, which takes the form:

$$Z_{t_{i-1}} = Z_{t_i} + h\Phi_i(Z_{t_i}) \quad (i = 1, 2, 3, \dots, N), \quad (16)$$

where h is the hyperparameter associated with the time step configuration, and $\Phi_i(Z_{t_i})$ denotes the incremental function of the Runge-Kutta method at step i . Since the time step in RF is uniform ($\Delta t_i = \Delta t_j$ for $i \neq j$), it can be simplified that $h = \Delta t_i (i = 0, 1, 2, \dots, N)$. And the $\Phi_i(Z_{t_i})$ is defined as:

$$\Phi_i(Z_{t_i}) = \sum_{j=1}^r b_j K_j^i(Z_{t_i}), \quad \text{where } K_s^i(Z_{t_i}) = v_\theta \left(Z_{t_i} - \Delta t_i \sum_{j=1}^{s-1} a_{sj} K_j^i, t_i - c_s \Delta t_i, \mathcal{P} \right). \quad (17)$$

In conjunction with Equation (16), the perturbed process can be represented as:

$$\tilde{Z}_{t_{i-1}} = \tilde{Z}_{t_i} + h \left[\Phi_i(\tilde{Z}_{t_i}) + \delta_i \right] \quad (i = 1, 2, 3, \dots, N), \quad \tilde{Z}_{t_N} = Z_{t_N} + \delta_N. \quad (18)$$

According to Runge [36], it is shown that for the 4-th order RF solver in this work:

$$|\Phi_i(y) - \Phi_i(x)| \leq \left[1 + \frac{Lh}{2!} + \frac{(Lh)^2}{3!} + \frac{(Lh)^4}{4!} \right] L|y - x|, \quad (19)$$

where L can be any Lipschitz constant of v . And from Equation (19), it can be obtained that

$$|\Phi_i(y) - \Phi_i(x)| \leq \Lambda|y - x|, \quad \text{for } 0 < h \leq h_0. \quad (20)$$

Take the $h_0 = 1/L$, it can be obtained that $\Lambda = (41/24)L$.

By subtracting the relations in Equation (16) from the corresponding ones in Equation (18) and by using the Equation (19), it can be obtained that

$$|\tilde{Z}_{t_{i-1}} - Z_{t_{i-1}}| \leq (1 + h\Lambda)|\tilde{Z}_{t_i} - Z_{t_i}| + h|\delta_{i-1}| \quad (i = 1, 2, 3, \dots, N). \quad (21)$$

As $(1 + h\Lambda)^n \leq e^{nh\Lambda}$, it can be iteratively obtained:

$$|\tilde{Z}_{t_0} - Z_{t_0}| \leq e^{\Lambda T} |\delta_0| + \frac{e^{\Lambda T} - 1}{\Lambda} \max_{1 \leq i \leq N} |\delta_i|. \quad (22)$$

B Additional Experimental Results

In this section, we provide additional experimental results to further demonstrate the effectiveness of the proposed method.

Algorithm 1: Visualization of Word-Pixel Response Maps for MM-DiT Architectures

Input: Input caption with k words $\mathcal{C} = \{w_1, \dots, w_k\}$, Target word index G **Output:** Word-pixel response maps $R = \{R_g | g \in G\}$

```
1  $z_{t_N} \leftarrow \mathcal{N}(0, \mathbf{I})$  // sample initial latent
2  $\mathcal{P} = \text{T5}(\mathcal{C})$  // compute prompt embedding
3  $A_{\text{cache}} \leftarrow \text{None}$  // initialize cached decoupled attention maps
4  $R \leftarrow []$ 
5 for  $i \leftarrow N$  to 1 do
6    $z_{t_{i-1}} \leftarrow z_{t_i} + (t_{i-1} - t_i) \cdot v_{\theta}^{\text{cache}}(z_{t_i}, t_i, \mathcal{P}, A_{\text{cache}})$ 
7    $A_{\text{cache}} \leftarrow A_{\text{cache}}/N$ 
8   for  $g \in G$  do
9      $A_g \leftarrow A_{\text{cache}}[:, g]$  // extract target attention maps
10     $A_g \leftarrow \text{resize}(A_g, H \times W)$  // resize to image resolution
11     $R.\text{append}(A_g)$ 
12 Function  $v_{\theta}^{\text{cache}}(z_{t_i}, t_i, \mathcal{P}, A_{\text{cache}})$ :
13   // multi-stream DiT blocks
14    $h_{\mathcal{C}} \leftarrow \text{AdaLayerNorm}(\mathcal{P}, t_i)$ 
15    $h_{\mathcal{I}} \leftarrow \text{AdaLayerNorm}(z_{t_i}, t_i)$ 
16   for  $l \leftarrow 1$  to  $L_{\text{multi}}$  do
17      $Q_{\mathcal{C}}, K_{\mathcal{C}}, V_{\mathcal{C}} \leftarrow W_{Q_{\mathcal{C}}}^l(h_{\mathcal{C}}), W_{K_{\mathcal{C}}}^l(h_{\mathcal{C}}), W_{V_{\mathcal{C}}}^l(h_{\mathcal{C}})$ 
18      $Q_{\mathcal{I}}, K_{\mathcal{I}}, V_{\mathcal{I}} \leftarrow W_{Q_{\mathcal{I}}}^l(h_{\mathcal{I}}), W_{K_{\mathcal{I}}}^l(h_{\mathcal{I}}), W_{V_{\mathcal{I}}}^l(h_{\mathcal{I}})$ 
19      $Q, K, V \leftarrow Q_{\mathcal{C}} \oplus Q_{\mathcal{I}}, K_{\mathcal{C}} \oplus K_{\mathcal{I}}, V_{\mathcal{C}} \oplus V_{\mathcal{I}}$ 
20      $M\{M_{\mathcal{C}\mathcal{C}}, M_{\mathcal{C}\mathcal{I}}, M_{\mathcal{I}\mathcal{C}}, M_{\mathcal{I}\mathcal{I}}\} \leftarrow \text{softmax}(\frac{QK^T}{\sqrt{\text{dim}}})$ 
21     if  $A_{\text{cache}}$  is None then
22        $A_{\text{cache}} \leftarrow M_{\mathcal{I}\mathcal{C}} + M_{\mathcal{C}\mathcal{I}}^T$ 
23     else
24        $A_{\text{cache}} \leftarrow A_{\text{cache}} + M_{\mathcal{I}\mathcal{C}} + M_{\mathcal{C}\mathcal{I}}^T$ 
25      $\{h_{\mathcal{C}}, h_{\mathcal{I}}\} \leftarrow M \cdot V$ 
26   // single-stream DiT blocks
27    $h \leftarrow h_{\mathcal{C}} \oplus h_{\mathcal{I}}$ 
28   for  $l \leftarrow 1$  to  $L_{\text{single}}$  do
29      $Q, K, V \leftarrow W_Q^l(h), W_K^l(h), W_V^l(h)$ 
30      $M\{M_{\mathcal{C}\mathcal{C}}, M_{\mathcal{C}\mathcal{I}}, M_{\mathcal{I}\mathcal{C}}, M_{\mathcal{I}\mathcal{I}}\} \leftarrow \text{softmax}(\frac{QK^T}{\sqrt{\text{dim}}})$ 
31      $A_{\text{cache}} \leftarrow A_{\text{cache}} + M_{\mathcal{I}\mathcal{C}} + M_{\mathcal{C}\mathcal{I}}^T$ 
32      $h \leftarrow M \cdot V$ 
33    $v_{t_i} \leftarrow \text{PostProcess}(h)$ 
34    $A_{\text{cache}} \leftarrow A_{\text{cache}}/(L_{\text{multi}} + L_{\text{single}})$ 
35   return  $v_{t_i}$ 
36 return  $R$ 
```

B.1 Additional Implementation Details

Visualization of Word-Pixel Response Maps². DAAM [41] is an attention visualization technique originally designed for UNet-based models, and thus cannot be directly applied to MM-DiT architectures. Inspired by DAAM, we visualize word-pixel response maps to validate the correctness of our proposed DDTA. As shown in Fig. 3, the visualization provides direct evidence that DDTA effectively decouples multimodal attention. The implementation details of the visualization are outlined in Algorithm 1.

²https://github.com/wmchen/vis_diffusion_attention

Algorithm 2: Semantic Editing Using RK Solver and DDTA

Input: Source image Z_{t_0} , Source prompt \mathcal{P}_s , Target prompt \mathcal{P}_t , r -order Butcher tableau \mathbf{B}_r , Sampling steps N , Index list for performing DDTA \mathbf{D}_{list}

Output: Target image \tilde{Z}_{t_0}

```
// Inversion Stage
1  $c \leftarrow N \times r$ 
2 for  $i \leftarrow 1$  to  $N$  do
3    $\Delta t_i \leftarrow t_i - t_{i-1}$ 
4    $Z_{t_i} \leftarrow Z_{t_{i-1}}$ 
5   for  $s \leftarrow 1$  to  $r$  do
6     if  $c$  in  $\mathbf{D}_{\text{list}}$  then
7        $K_s^i \leftarrow \text{DDTA}_{\text{save}} \left( Z_{t_{i-1}} + \Delta t_i \sum_{j=1}^{s-1} a_{sj} K_j^i, t_{i-1} + c_s \Delta t_i, \mathcal{P}_s \right)$ 
8     else
9        $K_s^i \leftarrow v_\theta \left( Z_{t_{i-1}} + \Delta t_i \sum_{j=1}^{s-1} a_{sj} K_j^i, t_{i-1} + c_s \Delta t_i, \mathcal{P}_s \right)$ 
10       $Z_{t_i} \leftarrow Z_{t_i} + b_s \Delta t_i K_s^i$ 
11       $c \leftarrow c - 1$ 

// Editing Stage
12  $\tilde{Z}_{t_N} \leftarrow Z_{t_N}$ 
13  $c \leftarrow 1$ 
14 for  $i \leftarrow N$  to 1 do
15    $\Delta t_i \leftarrow t_i - t_{i-1}$ 
16    $\tilde{Z}_{t_{i-1}} \leftarrow \tilde{Z}_{t_i}$ 
17   for  $s \leftarrow 1$  to  $r$  do
18     if  $c$  in  $\mathbf{D}_{\text{list}}$  then
19        $\tilde{K}_s^i \leftarrow \text{DDTA}_{\text{manipulate}} \left( \tilde{Z}_{t_i} - \Delta t_i \sum_{j=1}^{s-1} a_{sj} \tilde{K}_j^i, t_i - c_s \Delta t_i, \mathcal{P}_t \right)$ 
20     else
21        $\tilde{K}_s^i \leftarrow v_\theta \left( \tilde{Z}_{t_i} - \Delta t_i \sum_{j=1}^{s-1} a_{sj} \tilde{K}_j^i, t_i - c_s \Delta t_i, \mathcal{P}_t \right)$ 
22        $\tilde{Z}_{t_{i-1}} \leftarrow \tilde{Z}_{t_i} - b_s \Delta t_i \tilde{K}_s^i$ 
23        $c \leftarrow c + 1$ 
24 return  $\tilde{Z}_{t_0}$ 
```

Image Reconstruction Task. The sampling steps of each method are set to 30, except for VQAE. The hyperparameter settings for RF inversion follow the configuration in the literature [35], with controller guidance $\gamma = 0.5$, $\eta = 1.0$, starting time $s = 8$, and stopping time $\tau = 25$.

Text-Guided Semantic Editing Task. For DDIM-based methods, the guidance scales for the inversion and editing branches are set to 1.0 and 7.5, respectively. For RF inversion, we report the best editing results on the PIE-Bench dataset using controller guidance parameters $\gamma = 0.5$, $\eta = 0.9$, with a starting time $s = 0$ and stopping time $\tau = 6$. To minimize the impact of image resolution, we resize the images from the PIE-Bench dataset [16] to match the resolution used in the corresponding pre-trained baselines, *i.e.*, 512×512 for SD and 1024×1024 for FLUX. We perform text-guided semantic editing using Algorithm 2, where we set $\mathbf{D}_{\text{list}} = [1]$. In all single-stream DiT blocks, we replace the cross-attention maps $\{M_{\mathcal{C}\mathcal{I}}, M_{\mathcal{I}\mathcal{C}}\}$ and apply a mean operation to the value feature $V_{\mathcal{I}}$.

B.2 Additional Ablation Studies

(1) Ablation on Butcher Tableau. The Runge-Kutta method comprises a family of numerical solvers, each defined by a specific Butcher tableau. We report the results obtained using various Butcher tableaux, ranging from second-order to fourth-order solvers. For the second-order methods, we

Table 5: Ablation study on various Butcher tableaux from the second-order to fourth-order solvers.

Variant	Order	PSNR \uparrow	SSIM \uparrow	LPIPS \downarrow
Midpoint	2	22.17	0.7766	0.1903
Heun	2	24.00	0.8124	0.1534
Ralston	2	23.73	0.8096	0.1556
Kutta	3	23.98	0.8131	0.1497
Heun	3	22.48	0.7780	0.1936
Ralston	3	21.46	0.7611	0.2061
Houwen	3	21.11	0.7488	0.2270
SSPRK3	3	20.52	0.7364	0.2373
Classic	4	24.46	0.8197	0.1425
3/8-rule	4	25.68	0.8364	0.1241
Ralston	4	20.16	0.7258	0.2564

include the midpoint, Heun’s, and Ralston’s [31] methods, which are given by:

$$\mathbf{B}_{\text{midpoint}}^{(2)} = \begin{array}{c|cc} 0 & 0 & 0 \\ \frac{1}{2} & \frac{1}{2} & 0 \\ \hline & 0 & 1 \end{array}, \quad \mathbf{B}_{\text{Heun}}^{(2)} = \begin{array}{c|cc} 0 & 0 & 0 \\ 1 & 1 & 0 \\ \hline & \frac{1}{2} & \frac{1}{2} \end{array}, \quad \mathbf{B}_{\text{Ralston}}^{(2)} = \begin{array}{c|cc} 0 & 0 & 0 \\ \frac{2}{3} & \frac{2}{3} & 0 \\ \hline & \frac{1}{4} & \frac{3}{4} \end{array}.$$

For the third-order methods, we include the Kutta’s [19], Heun’s, Ralston’s [31], Van der Houwen’s [7], and Strong Stability Preserving Runge-Kutta (SSPRK3) methods, each defined as follows:

$$\mathbf{B}_{\text{Kutta}}^{(3)} = \begin{array}{c|ccc} 0 & 0 & 0 & 0 \\ \frac{1}{2} & \frac{1}{2} & 0 & 0 \\ 1 & -1 & 2 & 0 \\ \hline & \frac{1}{6} & \frac{2}{3} & \frac{1}{6} \end{array}, \quad \mathbf{B}_{\text{Heun}}^{(3)} = \begin{array}{c|ccc} 0 & 0 & 0 & 0 \\ \frac{1}{3} & \frac{1}{3} & 0 & 0 \\ \frac{2}{3} & 0 & \frac{2}{3} & 0 \\ \hline & \frac{1}{4} & 0 & \frac{3}{4} \end{array}, \quad \mathbf{B}_{\text{Ralston}}^{(3)} = \begin{array}{c|ccc} 0 & 0 & 0 & 0 \\ \frac{1}{2} & \frac{1}{2} & 0 & 0 \\ \frac{3}{4} & 0 & \frac{3}{4} & 0 \\ \hline & \frac{2}{9} & \frac{1}{3} & \frac{4}{9} \end{array},$$

$$\mathbf{B}_{\text{Houwen}}^{(3)} = \begin{array}{c|ccc} 0 & 0 & 0 & 0 \\ \frac{8}{15} & \frac{8}{15} & 0 & 0 \\ \frac{2}{3} & \frac{1}{4} & \frac{5}{12} & 0 \\ \hline & \frac{1}{4} & 0 & \frac{3}{4} \end{array}, \quad \mathbf{B}_{\text{SSPRK3}}^{(3)} = \begin{array}{c|ccc} 0 & 0 & 0 & 0 \\ 1 & 1 & 0 & 0 \\ \frac{1}{2} & \frac{1}{4} & \frac{1}{4} & 0 \\ \hline & \frac{1}{6} & \frac{1}{6} & \frac{2}{3} \end{array}.$$

For the fourth-order methods, we include the classic, 3/8-rule, and Ralston’s [31] methods, which are defined by:

$$\mathbf{B}_{\text{classic}}^{(4)} = \begin{array}{c|cccc} 0 & 0 & 0 & 0 & 0 \\ \frac{1}{2} & \frac{1}{2} & 0 & 0 & 0 \\ \frac{1}{2} & 0 & \frac{1}{2} & 0 & 0 \\ 1 & 0 & 0 & 1 & 0 \\ \hline & \frac{1}{6} & \frac{1}{3} & \frac{1}{3} & \frac{1}{6} \end{array}, \quad \mathbf{B}_{\text{3/8-rule}}^{(4)} = \begin{array}{c|cccc} 0 & 0 & 0 & 0 & 0 \\ \frac{1}{3} & \frac{1}{3} & 0 & 0 & 0 \\ \frac{2}{3} & -\frac{1}{3} & 1 & 0 & 0 \\ 1 & 1 & -1 & 1 & 0 \\ \hline & \frac{1}{8} & \frac{3}{8} & \frac{3}{8} & \frac{1}{8} \end{array},$$

$$\mathbf{B}_{\text{Ralston}}^{(4)} = \begin{array}{c|cccc} 0 & 0 & 0 & 0 & 0 \\ 0.4 & 0.4 & 0 & 0 & 0 \\ 0.45573725 & 0.29697761 & 0.15875964 & 0 & 0 \\ 1 & 0.21810040 & -3.05096516 & 3.83286476 & 0 \\ \hline & 0.17476028 & -0.55148066 & 1.20553560 & 0.17118478 \end{array}.$$

The comparison results of various Butcher tableaux are shown in Tab. 5. The Heun’s, Kutta’s, and 3/8-rule variants achieve the best performance from the second-order to the fourth-order solver. Among the second-order to the fourth-order solvers, the fourth-order solver achieves the best performance, while the third-order solver slightly outperforms the second-order method.

Table 6: Ablation study on sampling steps and NFEs (Number of Function Evaluations).

Method	Steps	NFEs	PSNR \uparrow	SSIM \uparrow	LPIPS \downarrow
Vanilla RF	30	60	17.46	0.5952	0.4282
Vanilla RF	60	120	19.03	0.6758	0.3092
Vanilla RF	90	180	19.53	0.6969	0.2841
Vanilla RF	120	240	17.70	0.6386	0.3539
RF-Solver	15	60	19.44	0.7157	0.2477
RF-Solver	30	120	22.20	0.7778	0.1890
RF-Solver	60	240	22.25	0.7655	0.2106
FireFlow	30	62	23.29	0.8006	0.1639
FireFlow	60	122	23.15	0.7861	0.1873
FireFlow	90	182	24.40	0.8146	0.1496
FireFlow	120	242	18.60	0.6543	0.3311
Ours ($r = 2$)	15	60	20.66	0.7393	0.2407
Ours ($r = 2$)	30	120	24.00	0.8124	0.1534
Ours ($r = 2$)	60	240	26.89	0.8607	0.0974
Ours ($r = 3$)	30	180	23.98	0.8131	0.1497
Ours ($r = 3$)	40	240	25.14	0.8274	0.1349
Ours ($r = 4$)	15	120	22.28	0.7699	0.1993
Ours ($r = 4$)	30	240	25.68	0.8364	0.1241

Table 7: Ablation study on the manipulation of different decoupled attention regions.

Attention Map				Attention Feature		Structure	Unedited Fidelity		CLIP Similarity	
M_{CC}	M_{II}	M_{CI}	M_{IC}	V_C	V_I	Distance \downarrow	PSNR \uparrow	SSIM \uparrow	Whole \uparrow	Edited \uparrow
\times	\times	\times	\times	\times	\times	0.0606	19.01	0.7540	25.97	23.27
\checkmark	\times	\times	\times	\times	\times	0.0610	19.02	0.7544	26.07	23.29
\times	\checkmark	\times	\times	\times	\times	0.0333	22.68	0.8234	25.19	22.50
\checkmark	\checkmark	\times	\times	\times	\times	0.0332	22.70	0.8236	25.17	22.51
\times	\times	\checkmark	\times	\times	\times	0.0606	19.04	0.7547	26.16	23.35
\times	\times	\times	\checkmark	\times	\times	0.0573	19.42	0.7630	25.93	23.16
\times	\times	\checkmark	\checkmark	\times	\times	0.0573	19.40	0.7625	25.98	23.16
\checkmark	\checkmark	\checkmark	\checkmark	\times	\times	0.0372	22.78	0.8249	25.20	22.50
\times	\times	\times	\times	\checkmark	\times	0.0589	19.28	0.7600	26.05	23.21
\times	\times	\times	\times	\times	\checkmark	0.0246	25.35	0.8530	24.73	22.17
\times	\times	\times	\times	\checkmark	\checkmark	0.0245	25.36	0.8532	24.71	22.13

(2) Ablation on Sampling Steps and Number of Function Evaluations. Although the high-order approximation improves reconstruction performance, it introduces additional Number of Function Evaluations (NFEs). For instance, our fourth-order RK solver with 30 sampling steps requires 240 NFEs, which is equivalent to a second-order method with twice the number of sampling steps. To rule out the possibility that the improvement is merely due to the increased NFEs, we conduct an ablation study on sampling steps and NFEs. The results are illustrated in Tab. 6. All experimental results indicate that increasing the number of sampling steps generally improves reconstruction performance. However, results on the vanilla RF and FireFlow [6] reveal that such performance gains do not scale indefinitely. Notably, the reconstruction performance degrades significantly when the number of sampling steps reaches 120. In addition, although the NFEs of vanilla RF with 120 sampling steps, RF-Solver [48] with 60 steps, FireFlow with 120 steps, our third-order RK solver with 40 steps, and our fourth-order RK solver with 30 steps are all about 240, our fourth-order method significantly outperforms the others. This demonstrates that the improvement in reconstruction performance is not solely owing to the increased NFEs.

(3) Ablation on Decoupled Attention. We conduct a comprehensive experiment to evaluate the influence of each attention region on the trade-off between fidelity and editability. In this experiment, we employ the third-order RK solver (Kutta’s variant) with 8 sampling steps as the sampler, and apply attention replacement only to the single-stream DiT blocks at the first timestep. From the results shown Tab. 7, we draw the following conclusions: (1) For self-attention maps, replacing M_{CC} yields only a very small improvement in both fidelity and editability, whereas replacing M_{II} significantly

Table 8: Ablation study on manipulation methods. Here, \mathcal{R} denotes the replacement operation, while \mathcal{M} indicates the mean operation.

M_{CC}	Attention Map			Attention Feature		Structure Distance↓	Unedited Fidelity		CLIP Similarity	
	M_{II}	M_{CI}	M_{IC}	V_C	V_I		PSNR↑	SSIM↑	Whole↑	Edited↑
\mathcal{R}	\times	\times	\times	\times	\times	0.0610	19.02	0.7544	26.07	23.29
\mathcal{M}	\times	\times	\times	\times	\times	0.0609	19.02	0.7542	26.07	23.32
\times	\mathcal{R}	\times	\times	\times	\times	0.0333	22.68	0.8234	25.19	22.50
\times	\mathcal{M}	\times	\times	\times	\times	0.0412	21.36	0.8010	25.61	22.51
\times	\times	\mathcal{R}	\times	\times	\times	0.0606	19.04	0.7547	26.16	23.35
\times	\times	\mathcal{M}	\times	\times	\times	0.0609	19.02	0.7544	26.11	23.28
\times	\times	\times	\mathcal{R}	\times	\times	0.0573	19.42	0.7630	25.93	23.16
\times	\times	\times	\mathcal{M}	\times	\times	0.0591	19.22	0.7593	26.04	23.28
\times	\times	\times	\times	\mathcal{R}	\times	0.0589	19.28	0.7600	26.05	23.21
\times	\times	\times	\times	\times	\mathcal{M}	0.0598	19.13	0.7567	26.07	23.25
\times	\times	\times	\times	\times	\mathcal{R}	0.0246	25.35	0.8530	24.73	22.17
\times	\times	\times	\times	\times	\mathcal{M}	0.0311	23.38	0.8312	25.26	22.53

Table 9: Computational cost of the proposed RK Solver.

Method	Order	NFEs	Runtime	GPU Memory
Vanilla RF	1	60	45.9	35.51
RK Solver	2	120	91.5	35.51
RK Solver	3	180	136.9	35.51
RK Solver	4	240	182.6	35.51

enhances fidelity at the cost of reduced editability. (2) Manipulating the two types of cross-attention maps leads to different effects, *i.e.*, replacing M_{CI} improves the editability while slightly enhancing the fidelity, whereas replacing M_{IC} improves the fidelity but slightly reduces the editability. (3) For the value attention features, replacing V_C slightly improves the fidelity while maintaining the editability, whereas replacing V_I significantly enhances the fidelity but substantially reduces the editability. Therefore, the order of contributions to fidelity is: $V_I > M_{II} > M_{IC} > M_{CI} > M_{CC}$, while the order of contributions to editability is: $M_{CI} > M_{CC} \approx V_C > M_{II} > V_I$.

(4) Ablation on Manipulation Method. We conduct a series of experiments to evaluate the effectiveness of different manipulation strategies. Experimental results in Tab. 8 show that the mean operation is slightly less effective than the replacement operation. Therefore, users can precisely control the edited image by customizing the manipulation method, the number of DiT blocks, and the sampling steps to achieve the most satisfactory results.

C Discussion

In this section, we discuss the societal impacts and computational cost of this work.

Broader Impact Statement. The proposed editing framework presents both positive and negative societal impacts. On the positive side, it enables relatively fine-grained and flexible editing of real-world images through simple modifications to textual descriptions, which may benefit applications in creative industries, digital art, and education. On the negative side, the method could be misused by malicious actors to generate inappropriate or offensive content. In particular, the high-order RK solver may exacerbate the inherent risks associated with the underlying generative models.

Computational Cost. Although our proposed framework achieves substantial improvements in both reconstruction and editing performance, it inevitably incurs additional computational overhead. Here, we present a quantitative analysis of the computational cost incurred by the proposed RK Solver and DDTA, reporting the runtime (in seconds per image) and GPU memory usage. In this evaluation, all experiments are conducted on a single NVIDIA L40 GPU, and the data is running under the bfloat16 floating-point format. The results of RK Solver, as shown in Tab. 9, lead to the following observations: (1) since the proposed method is training-free, all solvers occupy the same GPU memory, and (2) the runtime increases approximately linearly with the solver’s order, as higher-order solvers require more NFEs. To quantify the computational overhead introduced by DDTA, we evaluate the runtime and

Table 10: Computational cost of the proposed DDTA. Here, \mathcal{R} denotes the replacement operation, while \mathcal{M} indicates the mean operation.

M_{CC}	Attention Map			Attention Feature		Runtime	GPU Memory
	M_{II}	M_{CI}	M_{IC}	V_C	V_I		
\times	\times	\times	\times	\times	\times	35.6	35.51
\mathcal{R}	\times	\times	\times	\times	\times	55.4	36.89
\mathcal{M}	\times	\times	\times	\times	\times	55.3	36.89
\times	\mathcal{R}	\times	\times	\times	\times	108.7	38.39
\times	\mathcal{M}	\times	\times	\times	\times	111.8	38.39
\times	\times	\mathcal{R}	\times	\times	\times	56.3	36.89
\times	\times	\mathcal{M}	\times	\times	\times	56.3	36.89
\times	\times	\times	\mathcal{R}	\times	\times	56.3	36.89
\times	\times	\times	\mathcal{M}	\times	\times	56.3	36.89
\times	\times	\times	\times	\mathcal{R}	\times	51.6	36.89
\times	\times	\times	\times	\mathcal{M}	\times	51.8	36.89
\times	\times	\times	\times	\times	\mathcal{R}	51.7	36.89
\times	\times	\times	\times	\times	\mathcal{M}	51.9	36.89

GPU memory consumption under different attention manipulation strategies. As shown in Tab. 10, applying DDTA leads to additional computational cost in both runtime and GPU memory usage. This overhead is directly correlated with the dimensionality of the preserved attention maps or features, following the order: $M_{II} > M_{CI} = M_{IC} > M_{CC} > V_I > V_C$. It is worth noting that the additional cost originates from storing and reusing attention maps/features from the inversion branch. Therefore, the specific manipulation type (e.g., replace or mean) does not affect the computational overhead.